

ENSO regulation of far- and mid-infrared contributions to clear-sky OLR

Brian H. Kahn¹, Xianglei Huang², Graeme L. Stephens¹, William D. Collins^{3,4}, Daniel R. Feldman³, Hui Su¹, Sun Wong¹, and Qing Yue¹

¹Jet Propulsion Laboratory, California Institute of Technology, Pasadena, CA, USA

²Department of Climate and Space Science and Engineering, University of Michigan, Ann Arbor, MI, USA

³Climate and Ecosystem Division, Lawrence Berkeley National Laboratory, Berkeley, CA, USA

⁴Department of Earth and Planetary Science, University of California, Berkeley, CA, USA

Submitted to *Geophysical Research Letters* on June 30th, 2016

Corresponding Author: Brian H. Kahn, Jet Propulsion Laboratory, 4800 Oak Grove Drive, Mail Stop 233-302, Pasadena, CA, 91109, USA; Tel. 310-795-0960; Email: brian.h.kahn@jpl.nasa.gov

Key Point #1: ENSO modulated variations in tropical-extratropical mixing are observed in far-IR and 6.3 μm emission bands.

Key Point #2: The ratio of far- and mid-IR emission, and its temporal and spatial variations, are closely linked to the atmospheric circulation and water vapor abundance.

Key Point #3: The importance of the far-IR in the context of present-day moist tropical processes is highlighted.

This is the author manuscript accepted for publication and has undergone full peer review but has not been through the copyediting, typesetting, pagination and proofreading process, which may lead to differences between this version and the Version of Record. Please cite this article as doi: [10.1002/2016GL070263](https://doi.org/10.1002/2016GL070263)

Author Manuscript

Abstract

NASA Aqua-derived thermodynamic profiles, calculated spectral clear-sky outgoing longwave radiation (OLR), and vertical velocity fields from meteorological reanalyses are combined to determine the relative proportion of the far-infrared (FIR) and mid-infrared (MIR) spectral contributions to the total clear-sky OLR during different phases of ENSO. In the ascending branch of the tropical circulation, the spatial variance of upper tropospheric water vapor is shown to be larger during La Niña than El Niño and is consistent with zonal symmetry changes in the tropical waveguide and associated tropical-extratropical mixing. In the descending branch, upper tropospheric water vapor shows weaker coupling to lower layers that is evidenced by changes in the ratio of FIR to MIR in the clear-sky OLR. Diagnostics from the Geophysical Fluid Dynamics Laboratory (GFDL) AM3 model simulation are generally similar to satellite data but the ratio of FIR to MIR is 5–10% larger with respect to dynamic regime.

Author Manuscript

1. Introduction

The spread of climate sensitivity determined from climate GCMs remains large and varies by a factor of ~ 2.5 among climate models [IPCC, 2013]. Future changes in the global circulation are uncertain and are linked to an ensemble of moist atmospheric processes that are in turn coupled to the global circulation over a wide range of temporal and spatial scales [e.g., Sherwood *et al.*, 2010; Su *et al.*, 2014]. One pathway in which the clear-sky tropical atmosphere is thought to play a key role in controlling the global circulation response is through upper tropospheric (UT) moistening from convection and the modulation of the greenhouse effect [e.g., Ramanathan and Collins, 1991; Su *et al.*, 2006]. Sinha and Harries [1995] showed that the maximum greenhouse forcing from upper tropospheric (UT) water vapor (~ 200 – 600 hPa) is located in the 250 – 500 cm^{-1} spectral region. Global top-of-atmosphere (TOA) observations in the far-infrared (FIR >15 μm) spectral region are needed given the unambiguous moistening within the tropical UT [Soden *et al.*, 2005] and evidence for a “super greenhouse” effect in climate models [Stephens *et al.*, 2016]. There is also a need for more advanced climate observation strategies [Wielicki *et al.*, 2013] that include more complete coverage of Earth’s infrared spectrum.

Roughly half of the Earth’s surface and atmospheric radiation is emitted to space in the mid-infrared (MIR <15 μm or > 667 cm^{-1}) and the other half in the FIR [Harries *et al.*, 2008]. A vast majority of the UT emission in the MIR region originates from the 6.3

μm vibrational ν_2 band (1400–1650 cm^{-1}). Motivated by our investigation of moist UT processes, the proportion of FIR rotational band emission relative to the 6.3 μm emission can be expressed as a ratio of FIR/6.3 μm emission. The ratio is known to be highest in the moist tropical atmosphere and the cold, dry polar latitudes, while it is lowest in the clear and dry low and mid-latitudes [Clough *et al.*, 1992; Slingo *et al.*, 1997]. GCM comparisons with spectral OLR observations show that biases in discrete bands of a few hundred cm^{-1} in width may be several factors higher than the mean bias obtained from the full infrared spectrum. This result points to compensating modeling errors between different spectral regions [Huang and Ramaswamy, 2008; Huang *et al.*, 2014] and the importance of making spectral observations in the FIR to improve general circulation models (GCMs). Furthermore, the spectral variations of the FIR and MIR across the relevant time and spatial scales of the diurnal, seasonal, and inter-annual cycles remain poorly understood. There is a paucity of observations in the FIR [Cox *et al.*, 2007; Mlynarczyk *et al.*, 2006] with approximately 7 orders of magnitude more existing remote sensing observations in the MIR than the FIR.

Satellite-derived thermodynamic profiles, calculated spectral OLR observations using a radiative transfer model constrained by observations, and pressure velocity fields obtained from meteorological reanalyses are combined to quantify the proportion of FIR and MIR in the clear-sky radiative response to moistening and drying in the low latitudes. El Niño Southern Oscillation (ENSO) dominates the present-day inter-annual variability.

Based on the previous works of *Pierrehumbert and Yang* [1993], *Waugh and Polvani* [2000], and other studies that linked inter-annual variability with tropical-extratropical mixing processes, we hypothesize that ENSO modulates the relationship between UT moistening (drying) and large-scale dynamical regimes, and in turn, the spectral characteristics of clear-sky OLR. We explore these relationships and compare the combined satellite-reanalysis diagnostics to the output from the Geophysical Fluid Dynamics Laboratory (GFDL) AM3 climate general circulation model (GCM). We focus on two spectral regions with emission originating in the UT (FIR: 10–560 cm^{-1} , 6.3: 1400–1650 cm^{-1}). We use the ratio of FIR to 6.3 as a proxy for the relative contributions of each band to the total clear-sky OLR.

2. Data and Methodology

Well-characterized and validated temperature and water vapor profiles from the Atmospheric Infrared Sounder (AIRS) [*Chahine et al.*, 2006] Version 6 release are used within clear and partially cloudy conditions. Sea surface temperatures (T_{sfc}) are obtained from the real-time global analysis provided by the National Centers for Environmental Prediction (NCEP) and are matched to every AIRS footprint. Collocated Aqua AIRS and Clouds and the Earth's Radiant Energy System (CERES) observations are used to infer spectrally resolved clear-sky OLR at 10 cm^{-1} resolution spanning from 10–2000 cm^{-1} [*Chen et al.*, 2013]. Gridded monthly-averaged, 500 hPa pressure velocity fields at

1.25°×1.25° from the Modern Era Retrospective-Analysis for Research and Applications (MERRA) reanalysis [*Rienecker et al.*, 2011] are used to establish a link between water vapor, spectral OLR, and large-scale vertical motion on monthly time scales.

A total of ten years (2003–2012) of AIRS thermodynamic profiles, spectrally resolved OLR, and 500 hPa pressure velocity fields (ω_{500}) during the December-January-February (DJF) time period are investigated. The monthly composite Multivariate ENSO Index (MEI) [*Wolter and Timlin*, 2011] is used to identify the months when a moderate El Niño (MEI > +0.9, henceforth ‘ELNI’) or a moderate La Niña (MEI < -0.9, henceforth ‘LANI’) event occurred. Starting with a monthly averaged, globally gridded, and spectrally resolved OLR data set at 2°×2.5° resolution, the AIRS profiles, T_{sfc} , and ω_{500} are re-gridded to monthly data sets at the same spatial resolution. The clear-sky OLR from the AIRS Standard Level 2 product [*Susskind et al.*, 2012] is used to show the total clear-sky OLR, as the spectrally-resolved OLR data set contains only 97-98% of the total OLR between 10 cm⁻¹ and 2000 cm⁻¹. AIRS profiles are retained for clear-sky and partially cloudy regions for all pressure levels of “good” quality [c.f., *Yue et al.*, 2013; *Wong et al.*, 2015], while ω_{500} is averaged over all values of cloud fraction. *Zelinka and Harman* [2009] illustrate the physical reasoning for this approach since the UT moistening is a direct consequence of convective detrainment for an ensemble of discrete small-scale convective events. Thus, if ω_{500} is filtered for the same cloud fraction values

as AIRS profiles, the convective cores that are ultimately responsible for the adjacent clear-sky moistening will not be included.

For comparison purposes, the clear-sky flux is calculated for the same FIR and $6.3\mu\text{m}$ bands using 6-hourly output from the GFDL AM3 model simulations that are forced by observed SST from 2003 to 2012 using the radiative transfer model in *Chen et al.* [2013]. The AM3 model [[Donner et al., 2011](#)] is the latest atmospheric GCM developed by GFDL with a horizontal resolution of 2.5° longitude by 2° latitude and 48 vertical levels.

Prabhakara et al. [1979] and *Stephens* [1990] showed that imprints of the global circulation are obtained as deviations of column water vapor (w_{COL}) from a climatological average \bar{w}_{COL} that is approximated from binned values of T_{sfc} , and is expressed as $\hat{w}_{COL}=(w_{COL} - \bar{w}_{COL})/w_{COL}$. Positive (negative) values imply an excess (deficit) of water vapor and all terms are averaged at $2^\circ \times 2.5^\circ$ resolution. Similarly, in this work we define an analogous parameter between 150–400 hPa as a proxy for UT column water vapor as $\hat{w}_{UT}=(w_{UT} - \bar{w}_{UT})/w_{UT}$. Both \hat{w}_{COL} and \hat{w}_{UT} reflect vertical redistributions of moisture by circulation regime and spectral OLR variations. Other definitions of \hat{w}_{UT} with AIRS pressure levels as low as 700 hPa were considered but are generally similar with reduced structure in the relationships.

3. Results

The clear-sky total OLR generally increases with T_{sfc} and a weak dependence of OLR on w_{COL} is found for $T_{\text{sfc}} < 295$ K (Figs. 1a and 1b). The dependence however becomes much stronger for $T_{\text{sfc}} > 295$ K with a reduction in OLR of approximately $20\text{--}25$ Wm^{-2} across the observed range of w_{COL} at $T_{\text{sfc}} \approx 300$ K. Significant scatter is observed on either side of \bar{w}_{COL} . Although these results are in very close agreement with *Raval et al.* [1994; c.f. Fig. 5], the gradients in clear-sky OLR with w_{COL} appear to be sharper than inferred from the Earth Radiation Budget Experiment (ERBE) data that are possibly related to the smaller fields of view of both AIRS and CERES, better clear and cloudy sky discrimination, and improved instrumentation and processing algorithms.

A much broader amount of scatter is observed for w_{UT} especially for $T_{\text{sfc}} > 297$ K (Figs. 1c and 1d). The sharp increase in w_{UT} occurs over a very small increase in T_{sfc} and is marked by a dramatic decrease in clear-sky OLR. The ratio of the FIR ($10\text{--}560$ cm^{-1}) to the 6.3 μm MIR ($1400\text{--}1650$ cm^{-1}) water vapor bands with respect to clear-sky OLR is shown in Figs. 1e and 1f, with the largest ratios found in the coolest and driest regions of the extratropics and the tropical super greenhouse regions [*Stephens et al.*, 2016]. The high values of the ratio are consistent with the reduction in broadband OLR with increasing T_{sfc} due to the super-Clausius Clapeyron increase in w_{UT} through convective moistening [*Huang and Ramaswamy*, 2008; *Su et al.*, 2006]. (As an aside, we note that the ratio is high in the extratropics because of the frequency shift in Planck emission towards longer wavelengths). The largest ENSO differences occur for $T_{\text{sfc}} > 297$ K and

furthermore broader scatter is observed in LANI (Fig. 1c) than ELNI (Fig. 1d) at lower T_{sfc} .

The ratio of FIR/6.3 OLR increases with increasing w_{UT} and decreasing OLR (Fig. 1g and 1h). Of particular note is the amount of scatter in the ratio at a fixed value of clear-sky OLR. This scatter varies by 5–15% of the mean value of the ratio depending on the magnitude of OLR. The scatter is tied to variability in other geophysical factors such as temperature lapse rate [e.g., *Allan et al.*, 1999]. This demonstrates the absence of a unique relationship between clear-sky OLR and the contributions from the 6.3 μm and FIR bands. Moreover, variations of other parameters can produce a range of non-unique solutions that cause spectral OLR compensation within climate GCMs [*Huang et al.*, 2014]. An inspection of more limited time periods reveals that the scatter in the FIR/6.3 ratio broadens further, pointing to the importance of measuring the spectral OLR over a variety of temporal and spatial scales. Results for the GFDL model are shown in Fig. S1 and point to further reductions in clear-sky OLR, and increases in w_{UT} relative to Fig. 1, consistent with a FIR/6.3 ratio that is 5–10% larger than shown in Fig. 1. There is also subtle ENSO variability observed in the GFDL model (Fig. S1) but is structured somewhat differently than Fig. 1.

The spatial patterns of \hat{w}_{COL} and \hat{w}_{UT} derived from AIRS profile data over the 10-year DJF time period are shown in Fig. 2. The spatial pattern of \hat{w}_{COL} (Figs. 2b and 2d) agrees very well with *Stephens* [1990] showing convective moistening in the tropical

western Pacific, portions of the ITCZ, and extensive regions of the extratropical storm tracks. The spatial pattern of \widehat{w}_{UT} (Figs. 2a and 2c) is however greatly amplified and also spatially shifted compared to \widehat{w}_{COL} . In the tropical western Pacific, note that while the spatial pattern is quite similar with a larger magnitude, the total area encompassed by positive \widehat{w}_{UT} values is spatially larger, indicating that some regions simultaneously have $\widehat{w}_{UT} > 0$ and $\widehat{w}_{COL} < 0$. In the tropical eastern Pacific and Atlantic, however, the \widehat{w}_{UT} pattern is different than \widehat{w}_{COL} , implying that much of the tropical UT is very dry ($\widehat{w}_{UT} < 0$) even in the case of a moist column ($\widehat{w}_{COL} > 0$). The spatial distributions also suggest that the extratropics are more likely than the tropics to have a positive \widehat{w}_{UT} instead of \widehat{w}_{COL} . Results for the GFDL model (Fig. S2) show spatially similar patterns with slightly larger values of \widehat{w}_{COL} and reduced values of \widehat{w}_{UT} in the low and midlatitudes compared to Fig. 2. The ENSO variations in Figs. 2 and S2 are spatially similar; however, some differences in the extratropics are observed, and a larger ENSO variation found in the GFDL model.

The moist and dry anomalies are spatially redistributed with ENSO variations (LANI minus ELNI). Moistening occurs during LANI in the UT to the north and south of the tropical western Pacific warm pool region, in proximity of and to the south of Hawaii, the Caribbean Sea, and the north Atlantic tropics, while ELNI shows dramatic moistening in the central equatorial Pacific region near the dateline. The spatial redistributions are closely tied to redistributions of vertical ascent associated with shifting convection [e.g.,

Soden, 1997] and are clearly seen in ω_{500} fields [Su and Jiang, 2013; cf. Fig. S3]. In the tropical western Pacific, the ENSO anomalies of \widehat{w}_{UT} are spatially similar to \widehat{w}_{COL} but are significantly stronger in magnitude; this suggests strong vertical coupling between the UT and underlying atmospheric layers. However, in the tropical eastern Pacific, the variations of \widehat{w}_{UT} are different than \widehat{w}_{COL} suggesting (1) large changes in the vertical structure of the global circulation response with respect to ENSO variability and (2) much weaker vertical coupling between the UT and underlying atmospheric layers in the descending branch of the Walker circulation.

The equivalent total clear-sky OLR and FIR/6.3 ratio are shown in Fig. 3. The zonal symmetry is enhanced during ELNI [e.g., Webster and Holton, 1982; Waugh and Polvani, 2000] while the zonal asymmetry is enhanced in LANI. While the ENSO variations of the FIR/6.3 ratio demonstrate coherence, the spatial patterns are noisier than clear sky OLR variations and point to non-uniqueness in spectral OLR variations. Very few clear-sky data points populate the convectively active regions over tropical Africa and the Amazon in South America because of persistent cloudiness regardless of the phase of ENSO. Results for the GFDL model (Fig. S4) show reduced clear-sky OLR by 5–15 Wm^{-2} in the tropics and an increase in the FIR/6.3 ratio of 5–10% compared to Fig. 3.

The \widehat{w}_{UT} and \widehat{w}_{COL} are sorted by ω_{500} into 10 hPa d^{-1} bins in Figs. 4a and 4b (4d and 4e for GFDL), and are further subdivided into ELNI (red) and LANI (blue). The \widehat{w}_{UT} and

\hat{w}_{COL} both show increased moistening with ascent [Hallberg and Inamdar, 1993; Bony et al., 1997] and increased drying with descent. However, the rate of moistening and drying with respect to ω_{500} is a factor of 2–5 higher for \hat{w}_{UT} compared to \hat{w}_{COL} in Aqua data and shows the inherent sensitivity of UT water vapor to dynamical regime [Bony et al., 1997; Chouhrouh et al., 1998]. Similar sorting of \hat{w}_{UT} and \hat{w}_{COL} by ω_{500} is found for both ELNI and LANI although we caution that detecting subtle differences requires a much longer and statistically significant record of ENSO variations. Results for the GFDL models suggest a factor of 1.5–3 higher for \hat{w}_{UT} compared to \hat{w}_{COL} with somewhat greater differences between ELNI and LANI than the satellite data.

The variance of \hat{w}_{UT} and \hat{w}_{COL} is shown with the spread in the colored shading. There are three features to highlight. First, the variance in \hat{w}_{COL} is less than \hat{w}_{UT} . Second, the variance is significantly less in regions of ascent compared to descent. Third, the variance is fairly large yet nearly identical for ELNI and LANI in regions of descent. However, in regions of ascent, the variance is typically a factor of 1.5–2× higher during LANI for both \hat{w}_{UT} and \hat{w}_{COL} (Figs. 4a, 4b, 4d, and 4e) although the magnitude remains particularly small for \hat{w}_{COL} . On average, the variance is much larger in the descending branch of the tropical circulation but the magnitude of variance is generally similar between the phases of ENSO.

4. Discussion

Spectral observations in the FIR (mean and variance), especially in moist low-latitude regions, may yield additional insight on important mixing processes and impacts on the radiation budget that operate in climate models. *Pierrehumbert and Yang* [1993] showed that tropical mixing is likely dominated by cross-isentropic transport from diabatic heating of convective latent heat release and radiative cooling in clear [e.g., *Allan et al.*, 1999; *Feldman et al.*, 2008] and cloudy skies [e.g., *Mather et al.*, 2007]. GCMs are known to artificially diffuse small-scale structures that are generated by mixing processes [e.g., *Skamarock*, 2004] and in turn may inadvertently enhance meridional transport through the tropical mixing barrier [*Webster and Holton*, 1982]. This transport may lead to unrealistic spatial homogenization of small-scale humidity fields, and to excessive drying in the tropics and moistening in the extratropics.

Pierrehumbert and Yang [1993] emphasize how these mixing processes could modulate present-day climate variability and anthropogenic climate change. Global observations of the FIR at small spatial scales and with frequent revisits that resolve UT deep convective and clear-sky moist processes may help shed light on the nature of turbulent mixing processes in the UT.

Waugh and Polvani [2000] showed that subtropical intrusions into the tropics are less common in ELNI compared to LANI. The upper tropospheric westerlies are weaker during ELNI and imply less mixing between subtropical and extratropical air. A more zonally symmetric tropical waveguide is observed during ELNI, which is also observed

in vertically resolved water vapor [Blankenship and Wilheit, 2001], with small enhancements of moisture between $\pm 10^\circ\text{N/S}$ and drying between $\pm 10\text{--}20^\circ\text{N/S}$ between 200–600 hPa. The dependence of FIR/6.3 μm on ω_{500} is shown in Figs. 4c and 4f. Both ELNI and LANI show similar dependences in the relative contribution of the FIR with respect to ω_{500} . The differences in the variance of the ratios between ELNI and LANI are subtle but are more apparent in the GFDL model. Interestingly, this behavior does not map to the clear-sky OLR dependence (Fig. S5). A larger discrepancy in the mean clear-sky OLR in ascending regions compared to descending regions, and a larger discrepancy in the variance in descending regions compared to ascending regions, is noted between Aqua and GFDL.

Previously published works on tropical-extratropical mixing are consistent with the dependence of \hat{w}_{UT} and \hat{w}_{COL} variances on the phase of ENSO and further motivate spectral FIR measurements as additional observational constraints on tropical variability (cf. Fig. S6). Our analysis suggests that additional FIR measurements are warranted to further connect the tropical circulation and energy transport to present-day climate variability (e.g., ENSO) and future climate change [Stephens *et al.*, 2016]. This work emphasized the moderate ENSO variations during the 2003–2012 time period (no DJF occurrences in 2013 and 2014 met the MEI criteria). Future work will focus on the characterization of the strong ENSO event during 2015–2016 and the degree of similarity between moderate and strong ENSO events.

5. Summary

A record of NASA Aqua AIRS-derived thermodynamic profiles, spectral clear-sky OLR obtained from collocated AIRS and CERES observations, and mid-tropospheric vertical velocity from MERRA reanalysis are used to assess the relative roles of the far-infrared (FIR) and mid-infrared (MIR) spectral regions on the clear-sky tropical OLR. We reaffirm previous results that the FIR plays a dominant role over the warmest tropical oceans that contain rates of moistening that exceed those explained by simple Clausius-Clapeyron arguments.

Significant variations in ENSO are used as a proxy for present-day inter-annual variability to establish the relationship between moistening and drying as a function of dynamical regime, and in turn relate moisture changes to the magnitude of spectral OLR. In the ascending branch of the tropical circulation, the variance of upper tropospheric moisture is shown to be larger in the La Niña phase rather than the El Niño phase. This behavior is consistent with changes in the zonal symmetry of the tropical waveguide and associated tropical-extratropical mixing processes that control moisture variability. In the descending branch of the tropical circulation, the variations of upper tropospheric water vapor deviate significantly from lower atmospheric layers, suggesting weaker vertical coupling of moist processes. These behaviors were to first order reproduced in the GFDL AM3 model. However, small yet systematic differences in the FIR/6.3 ratio, clear-sky

OLR, upper tropospheric water vapor, and their variances with ENSO variability were described. Subtle discrepancies in the spectral OLR between satellite/reanalysis observations and the GFDL model, and their coupling to the atmospheric circulation, suggest the value of diagnostics linking radiation and dynamics.

Global scale spectral band observations in the FIR may help shed light on a wide range of upper tropospheric moist processes that are poorly characterized over a range of spatial and temporal scales. These moist processes are relevant in the context of current climate variability and potentially anthropogenic climate change that could lead to systematic changes in the dominant types of El Niño [Yeh *et al.*, 2009].

Acknowledgments

A portion of this research was carried out at the Jet Propulsion Laboratory (JPL), California Institute of Technology, under a contract with the National Aeronautics and Space Administration. We thank two anonymous reviewers for very constructive feedback and insights that led to an improved manuscript. B. Kahn was supported by Strategic University Research Partnership (SURP) proposal between JPL and the University of Michigan. X. Huang was supported by NASA under grant NNX14AJ50G awarded to the University of Michigan. D. Feldman and W. Collins acknowledge support by the U.S. Department of Energy, Office of Science, Office of Biological and Environmental Research, Terrestrial Ecosystem Science and Atmospheric System

Research programs, under award number DE-ACO2-05CH11231. The AIRS version 6 data sets were processed by and obtained from the Goddard Earth Services Data and Information Services Center (<http://daac.gsfc.nasa.gov/>). The MERRA data sets were processed by and obtained from the NASA Goddard's Global Modeling and Assimilation Office (GMAO). © 2016. All rights reserved. Government sponsorship acknowledged.

Author Manuscript

References

- Allan, R. P., K. P. Shine, A. Slingo, and J. A. Pamment (1999), The dependence of clear-sky outgoing long-wave radiation on surface temperature and relative humidity, *Q. J. R. Meteorol. Soc.*, **125**, 2103–2126.
- Blacker, C. B., and T. T. Wilheit (2001), SSM/T-2 measurements of regional changes in three-dimensional water vapor fields during ENSO events, *J. Geophys. Res.*, **106**, 5239–5254.
- Bony, S., K.-M. Lau, and Y. C. Sud (1997), Sea surface temperature and large-scale circulation influences on tropical greenhouse effect and cloud radiative forcing, *J. Climate*, **10**, 2055–2077.
- Chou, J.-P., A. Chédin, and N. A. Scott (1998), Relationship between sea surface temperature, vertical dynamics, and the vertical distribution of atmospheric water vapor inferred from TOVS observations, *J. Geophys. Res.*, **103**, 23,173–23,180.
- Chahine, M. T., T. S. Pagano, H. H. Aumann and Coauthors (2006), The Atmospheric Infrared Sounder (AIRS): Improving weather forecasting and providing new insights into climate, *Bull. Amer. Meteor. Soc.*, **87**, 911–926, doi: 10.1175/BAMS-87-7-911.
- Chen, X., X. Huang, N. G. Loeb, and H. Wei (2013), Comparisons of Clear-Sky Outgoing Far-IR Flux Inferred from Satellite Observations and Computed from the Three Most Recent Reanalysis Products. *J. Climate*, **26**, 478–494. doi: [10.1175/JCLI-D-12-00212.1](https://doi.org/10.1175/JCLI-D-12-00212.1)

- Chen, X., X. Huang, and X. Liu, 2013: Non-negligible effects of cloud vertical overlapping assumptions on longwave spectral fingerprinting studies. *J. Geophys. Res. Atmos.*, **118**, 7309–7320, doi:[10.1002/jgrd.50562](https://doi.org/10.1002/jgrd.50562).
- Crough, S. A., M. J. Iacono, and J.-L. Moncet (1992), Line-by-line calculations of atmospheric fluxes and cooling rates: Application to water vapor, *J. Geophys. Res.*, **97**, 15761–15785, doi: [10.1029/92JD01419](https://doi.org/10.1029/92JD01419).
- Cox, C. V., J. E. Murray, J. P. Taylor, P. D. Green, J. C. Pickering, J. E. Harries, and A. E. East (2007), Clear-sky far-infrared measurements observed with TAFTS during the EAQUATE campaign, September 2004, *Q. J. Royal. Met. Soc.*, **133**, 273–283.
- Donner, L. J., and Coauthors, 2011: The dynamical core, physical parameterizations, and basic simulation characteristics of the atmospheric component AM3 of the GFDL global coupled model CM3. *J. Climate*, **24**, 3484–3519, doi:[10.1175/2011JCLI3955.1](https://doi.org/10.1175/2011JCLI3955.1).
- Feldman, D. R., K. N. Liou, R. L. Shia, and Y. L. Yung (2008), On the information content of the thermal infrared cooling rate profile from satellite instrument measurements, *J. Geophys. Res.*, **113**, D11118, doi: [10.1029/2007JD009041](https://doi.org/10.1029/2007JD009041).
- Hallberg, R., and A. K. Inamdar (1993), Observations of seasonal variations in atmospheric greenhouse trapping and its enhancement at high sea surface temperature, *J. Climate*, **6**, 920–931.

Harries, J., B. Carli, R. Rizzi, C. Serio, M. Mlynchzak, L. Palchetti, T. Maestri, H.

Brindley, and G. Masiello (2008), The far-infrared Earth, *Rev. Geophys.*, **46**,

RG4004, doi: [10.1029/2007RG000233](https://doi.org/10.1029/2007RG000233).

Huang, X., X. Chen, G. L. Potter, L. Oreopoulos, J. N. S. Cole, D. Lee, and N. G. Loeb

(2014), A Global Climatology of Outgoing Longwave Spectral Cloud Radiative

Effect and Associated Effective Cloud Properties. *J. Climate*, **27**, 7475–7492, doi:

[10.1175/JCLI-D-13-00663.1](https://doi.org/10.1175/JCLI-D-13-00663.1)

Huang, Y., and V. Ramaswamy (2008), Observed and simulated seasonal co-variations of

outgoing longwave radiation spectrum and surface temperature, *Geophys. Res. Lett.*,

35, L17803, doi:10.1029/2008GL034859.

IPCC (2013), *Climate Change 2013: The Physical Science Basis. Contribution of*

Working Group I to the Fifth Assessment Report of the Intergovernmental Panel on

Climate Change [Stocker, T.F., D. Qin, G.-K. Plattner, M. Tignor, S.K. Allen, J.

Boschung, A. Nauels, Y. Xia, V. Bex and P.M. Midgley (eds.)]. Cambridge

University Press, Cambridge, United Kingdom and New York, NY, USA, 1535 pp,

doi: [10.1017/CBO9781107415324](https://doi.org/10.1017/CBO9781107415324).

Mather, J. H., S. A. McFarlane, M. A. Miller, and K. L. Johnson (2007), Cloud properties

and associated radiative heating rates in the tropical western Pacific, *J. Geophys. Res.*,

112, D05201, doi: [10.1029/2006JD007555](https://doi.org/10.1029/2006JD007555).

Author Manuscript

- Mlynczak, M. G., et al. (2006), First light from the Far-Infrared Spectroscopy of the Troposphere (FIRST) instrument, *Geophys. Res. Lett.*, **33**, L07704, doi: 10.1029/2005GL025114.
- Pierrehumbert, R. T., and H. Yang (1993), Global chaotic mixing on isentropic surfaces, *J. Atmos. Sci.*, **50**, 2462–2480.
- Prabhakara, C., G. Dalu, R. C. Lo, and N. R. Nath (1979), Remote sensing of seasonal distribution of precipitable water vapor over the oceans and the inference of boundary-layer structure, *Mon. Wea. Rev.*, **107**, 1388–1401.
- Ramanathan, V., and W. Collins (1991), Thermodynamic regulation of ocean warming by cirrus clouds deduced from observations of the 1987 El Niño, *Nature*, **351**, 27–32.
- Raval, A., and V. Ramanathan (1989), Observational determination of the greenhouse effect, *Nature*, **342**, 758–761.
- Raval, A., A. H. Oort, and V. Ramaswamy (1994), Observed dependence of outgoing longwave radiation on sea surface temperature and moisture, *J. Climate*, **7**, 807–821.
- Rienecker, M.M., M.J. Suarez, R. Gelaro, and Coauthors (2011), MERRA: NASA's Modern-Era Retrospective Analysis for Research and Applications. *J. Climate*, **24**, 3624–3648, doi: 10.1175/JCLI-D-11-00015.1.
- Sherwood, S. C., R. Roca, T. M. Weckwerth, and N. G. Andronova (2010), Tropospheric water vapor, convection, and climate, *Rev. Geophys.*, **48**, RG2001, doi: 10.1029/2009RG000301.

Sinha, A., and J. E. Harries (1995), Water vapour and greenhouse trapping: The role of far infrared absorption, *Geophys. Res. Lett.*, **22**, 2147–2150.

Skamarock, W. C. (2004), Evaluating mesoscale NWP models using kinetic energy spectra, *Mon. Wea. Rev.*, **132**, 3019–3032.

Slingo, A., and M. J. Webb (1997), The spectral signature of global warming, *Q. J. Royal Met. Soc.*, **123**, 293–307.

Soden, B. J. (1997), Variations in the tropical greenhouse effect during El Niño, *J. Climate*, **10**, 1050–1055.

Soden, B. J., D. L. Jackson, V. Ramaswamy, M. D. Schwarzkopf, and X. Huang (2005), The radiative signature of upper tropospheric moistening, *Science*, **310**, 841–844.

Stephens, G. L. (1990), On the relationship between water vapor over the oceans and sea surface temperature, *J. Climate*, **3**, 634–645.

Stephens, G. L., B. H. Kahn, and M. Richardson (2016), The super greenhouse effect in a changing climate, *J. Climate*, **29**, 5469–5482, doi:10.1175/JCLI-D-15-0234.1.

Su, H., W.G. Read, J. H. Jiang, J.W. Waters, D.L. Wu, and E.J. Fetzer (2006), Enhanced positive water vapor feedback associated with tropical deep convection: New evidence from Aura MLS, *Geophys. Res. Lett.*, **33**, L05709, doi:10.1029/2005GL025505.

Su, H., J. H. Jiang, C. Zhai, T. J. Shen, J. D. Neelin, G. L. Stephens, and Y. L. Yung (2014), Weakening and strengthening structures in the Hadley Circulation change

under global warming and implications for cloud response and climate sensitivity, *J. Geophys. Res.*, **119**, 5787–5805, doi: 10.1002/2014JD021642.

Su, H., and J.H. Jiang (2013), Tropical clouds and circulation changes during the 2006-07 and 2009-10 El Niños, *J. Climate*, **26**, 399–413, doi:10.1175/JCLI-D-12-00152.1.

Suskind, J., G. Molnar, L. Iredell, and N. G. Loeb (2012), Interannual variability of outgoing longwave radiation as observed by AIRS and CERES, *J. Geophys. Res.*, **117**, D23107, doi:10.1029/2012JD017997.

Wang, D. W., and L. M. Polvani (2000), Climatology of intrusions into the tropical upper troposphere, *Geophys. Res. Lett.*, **27**, 3857–3860.

Webster, P. J., and J. R. Holton (1982), Cross-equatorial response to middle-latitude forcing in a zonally varying basic state, *J. Atmos. Sci.*, **39**, 722–733.

Wielicki, B. A., D. F. Young, M. G. Mlynchak and Coauthors (2013), Achieving climate change absolute accuracy in orbit, *Bull. Amer. Met. Soc.*, **94**, 1519–1539.

Wolter, K., and M. S. Timlin (2011), El Niño/Southern Oscillation behavior since 1871 as diagnosed in an extended multivariate ENSO index (MEI.ext), *Int. J. Clim.*, **31**, 1074–1087.

Wong, S., E. J. Fetzer, M. Schreier, and F. W. Irion (2015), Cloud-induced uncertainties in temperature and specific humidity, *J. Geophys. Res.*, **120**, doi: 10.1002/2014JD022440.

Author Manuscript

G. Manion, E. F. F.

AIRS and ECMWF

Yeh, S.-W., J.-S. Kug, B. Dewitte, M.-H. Kwon, B. P. Kirtman, and F.-F. Jin (2009), El Niño in a changing climate, *Nature*, **461**, 511–515.

Yue, Q., E. J. Fetzer, B. H. Kahn, S. Wong, G. Manion, A. Guillaume, and B. Wilson (2013), Cloud-state dependent sampling in AIRS observations based on CloudSat cloud classification, *J. Climate*, **26**, 8357–8377.

Zelinka, M. D., and D. L. Hartmann (2009), Response of humidity and clouds to tropical deep convection, *J. Climate*, **22**, 2389–2404.

Author Manuscript

List of Figures

Figure 1. (a and b) Scatter plot of w_{COL} (mm) versus sea surface temperature (T_{sfc}) over clear-sky oceans that are limited to regions with $T_{sfc} > 280$ K for warm (right column) and cold (left column) phases of ENSO. The color scale is the clear-sky OLR (Wm^{-2}). Each point represents a 10-year DJF average at $2^\circ \times 2.5^\circ$ spatial resolution. The gray line is \bar{w}_{COL} following Stephens (1990) and Prabhakara et al. (1979) and is an average for each T_{sfc} bin. (c and d) Similar to the upper left except for w_{UT} . (e and f) Clear-sky OLR versus T_{sfc} as a function of FIR/6.3. (g and h) Broadband clear-sky OLR versus FIR/6.3 OLR as a function of w_{UT} .

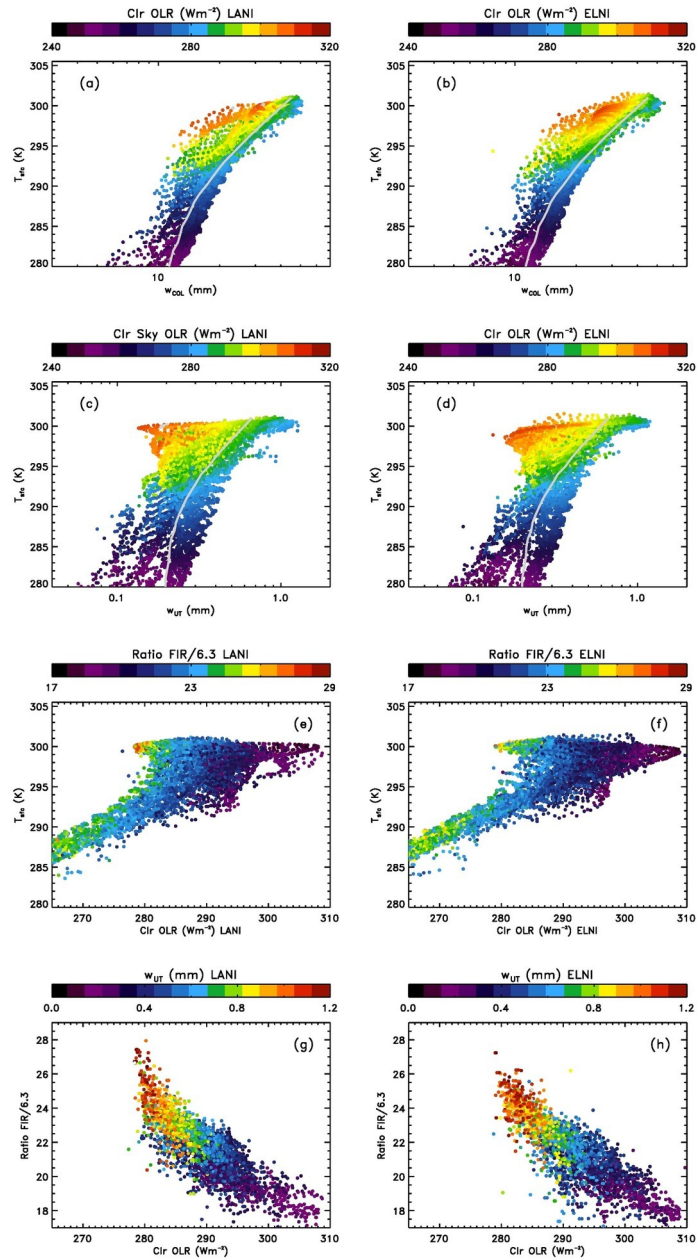
Figure 2. Shown are spatial maps of (a and c) \hat{w}_{UT} and (b and d) \hat{w}_{COL} for the 10-year DJF record. LANI (ELNI) is in the upper (middle) row, and LANI-ELNI differences are in the lower row.

Figure 3. Shown are spatial maps of (a and c) clear-sky OLR from the AIRS Standard L2 product and (b and d) FIR/6.3 μm ratio from the spectrally-resolved OLR calculation for the 10-year DJF record. LANI (ELNI) is in the upper (middle) row, and LANI-ELNI differences are in the lower row.

Figure 4. Shown is (a) \hat{w}_{COL} , (b) \hat{w}_{UT} , and (c) FIR/6.3 μm ratio as a function of MERRA ω_{500} during ELNI (red) and LANI (blue). The $\pm 1\sigma$ standard deviation of the monthly data within each ω_{500} bin is shown as the spread in the shading. The dashed lines

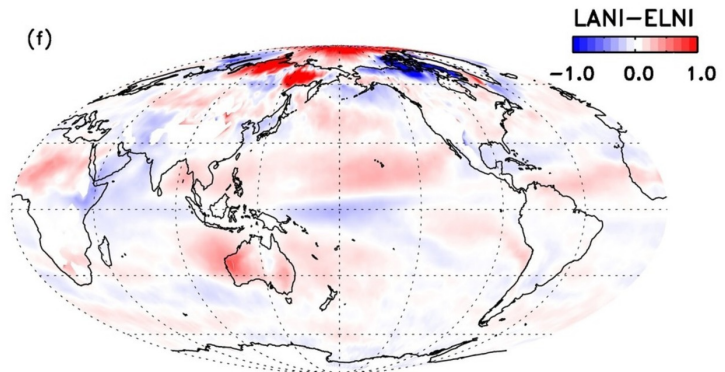
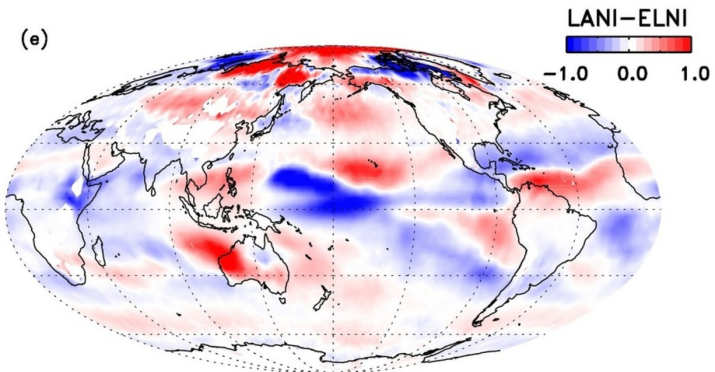
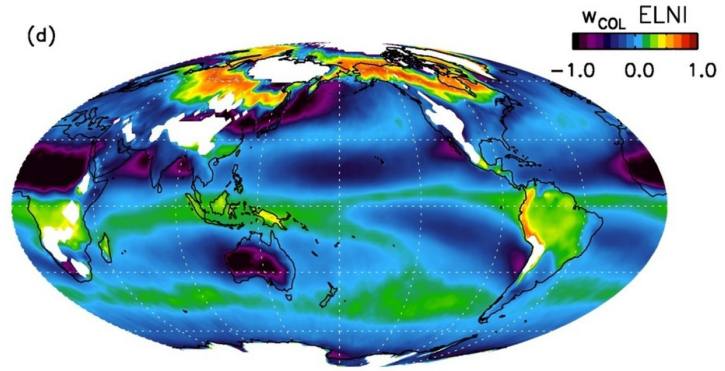
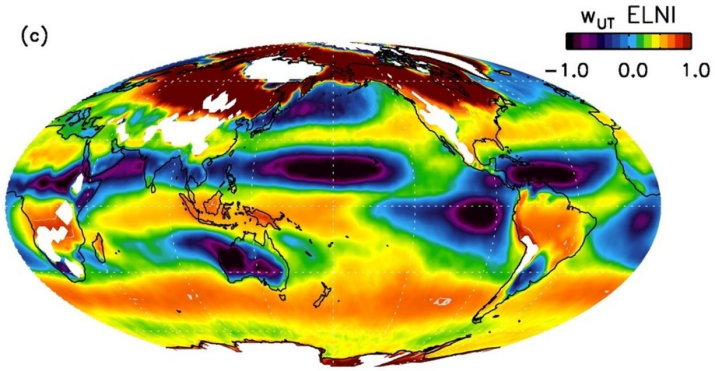
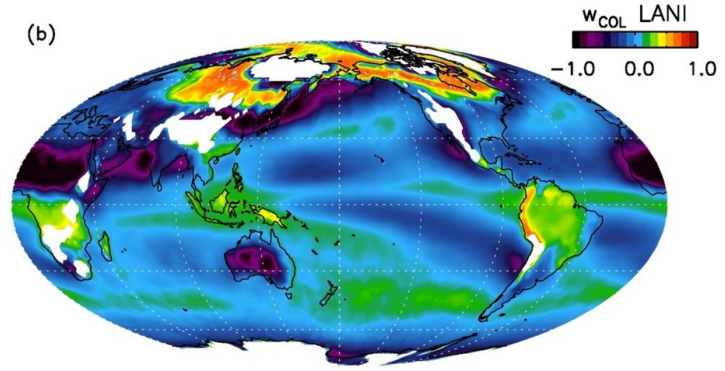
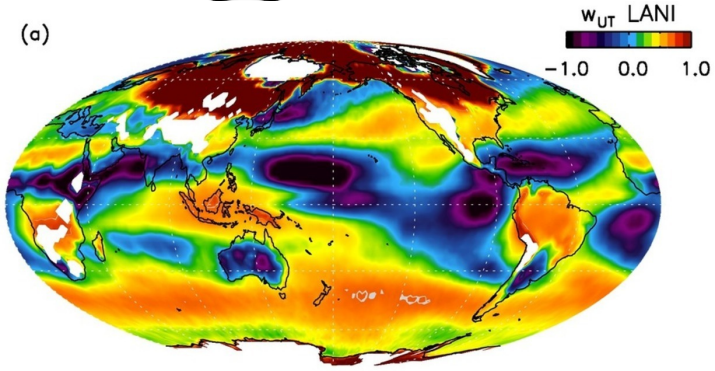
show the numbers of counts within each ω_{500} bin. Panels (d)-(f) are identical to (a)-(c) except for the GFDL AM3 model.

Author Manuscript



2016GL070263-f01-z-.jpg

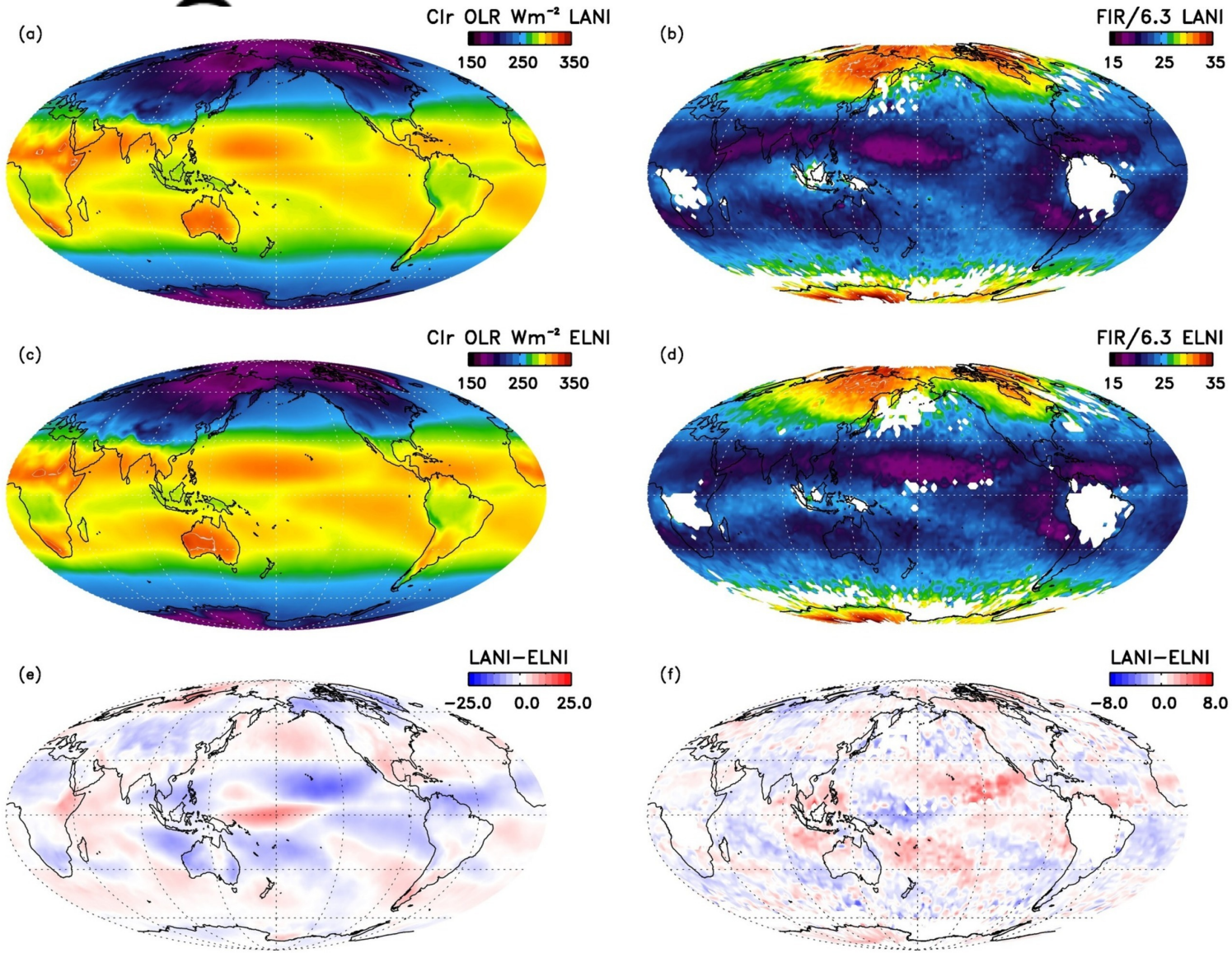
rt



A

2016GL070263-f02-z-.jpg

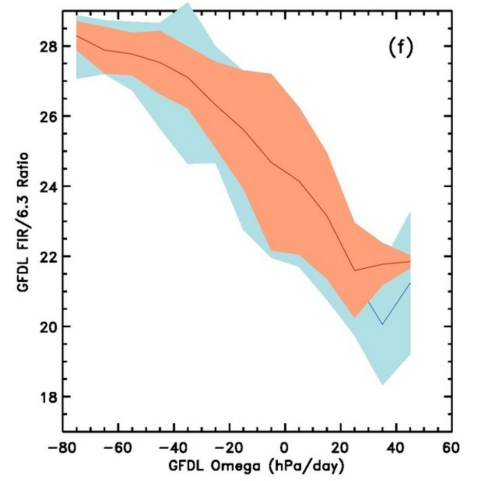
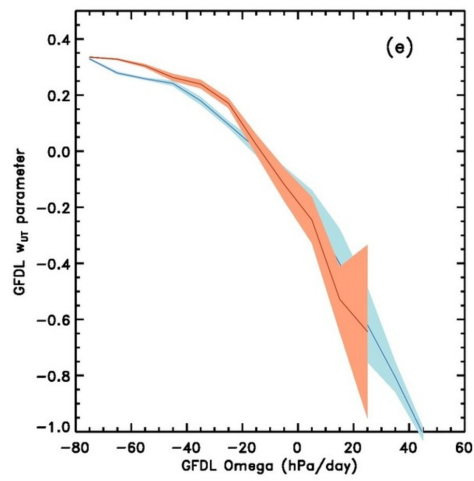
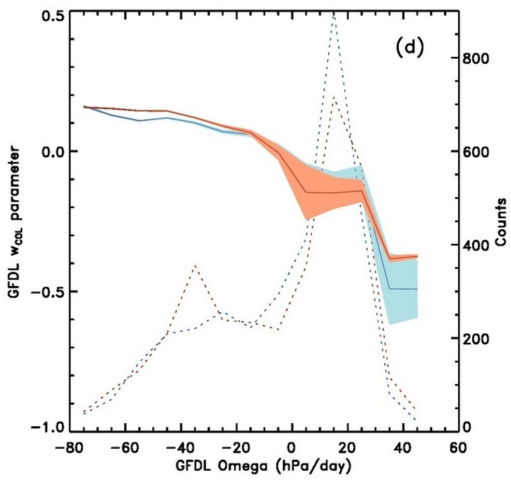
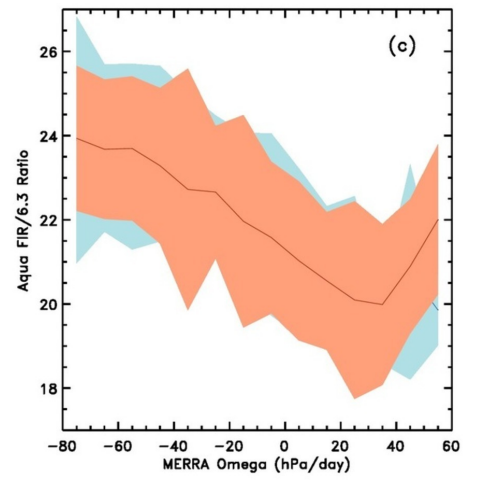
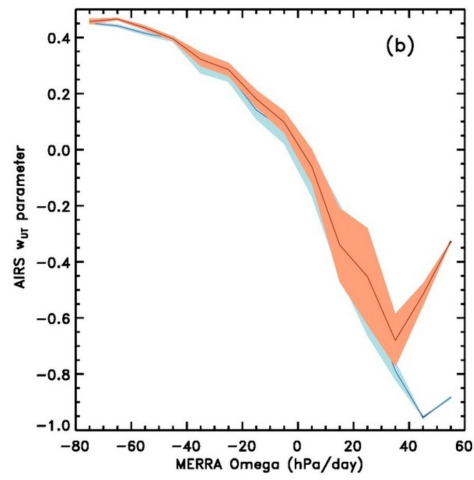
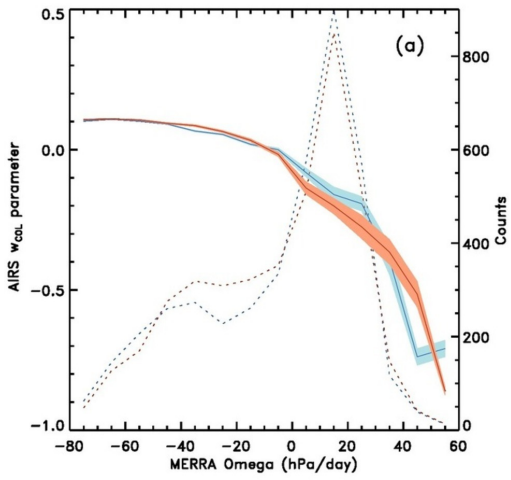
rt



A

2016GL070263-f03-z-.jpg

pt



Al

2016GL070263-f04-z-.jpg